

Magnon spin-current theory for the longitudinal spin-Seebeck effectS. M. Rezende,^{1,*} R. L. Rodríguez-Suárez,² R. O. Cunha,¹ A. R. Rodrigues,¹ F. L. A. Machado,¹ G. A. Fonseca Guerra,¹ J. C. Lopez Ortiz,¹ and A. Azevedo¹¹*Departamento de Física, Universidade Federal de Pernambuco, 50670-901, Recife, Pernambuco, Brasil*²*Facultad de Física, Pontificia Universidad Católica de Chile, Casilla 306, Santiago, Chile*

(Received 8 September 2013; revised manuscript received 27 December 2013; published 15 January 2014)

We present a theoretical model for the longitudinal spin-Seebeck effect (LSSE) in bilayers made of a ferromagnetic insulator (FMI), such as yttrium iron garnet (YIG), and a normal metal (NM), such as platinum (Pt), that relies on the bulk magnon spin current created by the temperature gradient across the thickness of the FMI. We show that the spin current pumped into the NM layer by the magnon accumulation in the FMI provides continuity of the spin current at the FMI/NM interface and is essential for the existence of the longitudinal spin-Seebeck effect. The results of the theory are in good agreement with experimental data for the variation of the LSSE with the sample temperature and with the FMI layer thickness in YIG/Pt bilayers.

DOI: [10.1103/PhysRevB.89.014416](https://doi.org/10.1103/PhysRevB.89.014416)

PACS number(s): 75.76.+j, 75.30.Ds, 85.75.-d, 85.80.-b

I. INTRODUCTION

Recent discoveries of phenomena involving the interaction of heat currents and spin currents has originated a vigorous field of spintronics, known as spin caloritronics [1]. One feature of this new field is that experiments have been leading theory; i.e., most experimental observations have been made before any theoretical prediction. This is the case of the spin-Seebeck effect (SSE), discovered in 2008, that consists of the generation of a spin current by a temperature gradient applied to a magnetic material [2]. In a few years, the SSE and other spin-dependent thermoelectric effects have been observed in many metallic, semiconductor, and insulating ferromagnets in several configurations and material structures [2–30]. This has stimulated intense theoretical effort [31–47] to explain the experimental observations and to put forward new ideas leading to a rapid evolution of the field. The attention drawn by the spin-dependent thermoelectric effects, and SSE in particular, is largely because they have revealed new mechanisms for generating and detecting spin currents, thus opening many possibilities in spintronics.

Depending on the experimental arrangement, the spin current generated by the SSE can be perpendicular or parallel to the temperature gradient, characterizing the so-called transverse [1–4] or longitudinal [1,5,6] configurations, respectively. While the transverse SSE can be observed in both metallic and insulating magnetic materials, the longitudinal spin-Seebeck effect (LSSE) is observed unambiguously only in insulators, because they are free from the anomalous Nernst effect [6,26,29]. The most common way to detect the spin currents generated by the SSE consists of measuring the voltage resulting from the charge current created by means of the inverse spin-Hall effect (ISHE) in a nonmagnetic metallic (NM) layer in contact with the magnetic material [48–52]. Other ways to observe the SSE involve the action of torques created by spin currents on the spin dynamics [10,15,21,23,24,37].

One striking feature of the SSE is that different types of materials and configurations reveal a variety of aspects of

the phenomenon, requiring different mechanisms to explain the generation of spin current by the thermal gradient. The pioneering experiments of Uchida *et al.* [2], with a temperature gradient along a permalloy film, were explained in terms of a nonuniform spin accumulation created along the film [1,2,31–35]. This produces a varying spin current transverse to the gradient and consequently a varying ISHE voltage in the attached NM strips. Similar experiments with the insulating ferrimagnet yttrium iron garnet ($\text{Y}_3\text{Fe}_5\text{O}_{12}$, or YIG) done with the same transverse configuration require another mechanism, since in insulators, the spin currents are carried by spin waves, or magnons. As shown in Refs. [1,3,38,45], the transverse spin currents are created by interfacial thermal spin pumping caused by the difference between the magnon temperature in the ferromagnet and the lattice temperature in the attached NM strips. The interfacial spin pumping is thermally activated by the temperature difference that varies along the film, resulting in a varying ISHE voltage. The same mechanism is believed to be operative in the longitudinal configuration, where the temperature gradient is applied across the thickness of the film [1,45]. However, while the calculated interfacial thermal spin pumping ISHE voltage is in reasonable agreement with the measured values in the transverse configuration, a few microvolts for a few Kelvin temperature difference, there has been no clear-cut comparison of theory with experiments for the longitudinal configuration.

In this paper, we propose a different mechanism for the LSSE that originates in the magnon flow across the thickness of the ferromagnetic insulator (FMI) film created by the temperature gradient. The proposed mechanism relies on the magnon spin current generated in the bulk of the film, not at the interface, but it requires the contact with a NM layer to provide continuity for the spin flow. The bulk spin current is calculated macroscopically with the Boltzmann equation for the magnon flow, subject to the appropriate boundary condition at the FMI/NM interface in a treatment similar to one used by Zhang and Zhang [53,54]. However, instead of using the concept of spin convertance introduced by Zhang and Zhang, we employ the familiar spin mixing conductance used to explain the spin pumping process in ferromagnetic metal/NM interfaces [55,56] and recently shown to hold in bilayers of YIG/platinum (Pt) [57]. In order to test key features

*Corresponding author: rezende@df.ufpe.br

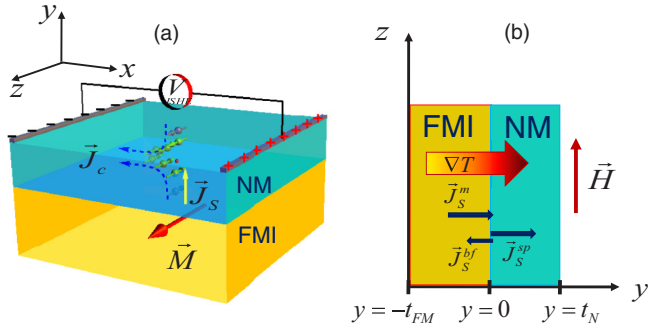


FIG. 1. (Color online) FMI/NM bilayer used to investigate the LSSE. (a) Illustration of the conversion of the spin into the charge current by the ISHE in the NM layer. (b) Coordinate axes used to calculate the spin currents generated by a temperature gradient perpendicular to the plane of the bilayer.

of the model, we have carried out experiments to measure the temperature dependence of the longitudinal SSE in YIG/Pt bilayers. The results of the model explain quantitatively our experimental data, as well recent measurements of the YIG thickness dependence of the LSSE in YIG/Pt bilayers [58].

The paper is organized as follows. Section II presents the derivation of the expression for the spin current in the FMI layer using the Boltzmann transport equation and the concept of magnon accumulation [53,54]. Section III is devoted to the calculation of the spin current at the FMI/NM interface using the pumped spin current into the NM layer, the condition of continuity of the current, and the expression for the ISHE voltage generated in the NM layer. In Sec. IV, the SSE spin current is calculated for YIG/Pt bilayers. Section V describes the experimental measurements and comparison with the results of the model. In the Appendix, we calculate the relaxation of magnons in YIG due to 4-magnon processes used in Sec. IV.

II. MAGNON SPIN CURRENT IN THE FMI LAYER

Consider the FMI/NM bilayer, illustrated in Fig. 1, in the presence of a temperature gradient normal to the plane and with a static magnetic field H applied in the plane. We chose a coordinate system with the z axis parallel to the field and the y axis perpendicular to the plane. In this section, we calculate the expression for the spin current in the FMI layer. The spin current in the FMI is carried by the magnetic excitations, which are spin waves, or magnons [53,54,59–61], with the wave vector \vec{k} and energy $\hbar\omega_k$. We denote by n_k the number of magnons with wave number k in the whole volume V of the FMI layer; n_k^0 the number in thermal equilibrium, given by the Bose-Einstein distribution, $n_k^0 = 1/[\exp(\hbar\omega_k/k_B T) - 1]$; and $\delta n_k = n_k - n_k^0$ the number in excess of equilibrium. The magnon accumulation δn_m is defined as the density of magnons in excess of equilibrium [53,54]:

$$\delta n_m = \frac{1}{(2\pi)^3} \int d^3k (n_k - n_k^0). \quad (1)$$

The magnon spin-current density with polarization z , \vec{J}_S^z , related to the magnetization current \vec{J}_M^z used in Refs. [59–61]

by $\vec{J}_S^z = \vec{J}_M^z/\gamma$, can be written as [53,54]

$$\vec{J}_S^z = \frac{\hbar}{(2\pi)^3} \int d^3k \vec{v}_k (n_k - n_k^0), \quad (2)$$

where $\gamma = g\mu_B/\hbar$ is the gyromagnetic ratio and \vec{v}_k is the k -magnon velocity. The distribution of the magnon number under the influence of the thermal gradient can be calculated with the Boltzmann transport equation. In the absence of external forces and in the relaxation approximation, in steady state it gives

$$n_k(\vec{r}) - n_k^0 = -\tau_k \vec{v}_k \cdot \nabla n_k(\vec{r}), \quad (3)$$

where τ_k is the k -magnon relaxation time. Using Eq. (3) in Eq. (2), one can show that the spin current is the sum of two parts, $\vec{J}_S^z = \vec{J}_{S\nabla T}^z + \vec{J}_{S\delta n}^z$, where

$$\vec{J}_{S\nabla T}^z = -\frac{\hbar}{(2\pi)^3} \int d^3k \tau_k \frac{\partial n_k^0}{\partial T} \vec{v}_k (\vec{v}_k \cdot \nabla T) \quad (4)$$

is the contribution of the temperature gradient and

$$\vec{J}_{S\delta n}^z = -\frac{\hbar}{(2\pi)^3} \int d^3k \tau_k \vec{v}_k (\vec{v}_k \cdot \nabla \delta n_k(\vec{r})) \quad (5)$$

is due to the spatial distribution of the magnon accumulation. With the temperature gradient normal to the plane, Eq. (4) gives the spin current in the y direction as

$$J_S^z = -S_S^z \frac{\partial T}{\partial y}, \quad (6)$$

$$S_S^z = \frac{\hbar}{(2\pi)^3 T} \int d^3k \tau_k v_{ky}^2 \frac{e^x x}{(e^x - 1)^2}, \quad (7)$$

where T is the average temperature and $x = \hbar\omega_k/k_B T$ is the normalized magnon energy. We consider the magnon and phonon systems to have the same temperature T , as recently demonstrated experimentally [30]. In order to calculate the spin current due to the gradient in the magnon accumulation, in the spirit of linear response theory, we follow Refs. [53,54] and write the distribution function as the sum of the equilibrium distribution plus a small deviation in the form of the following expansion:

$$n_k(\vec{r}) = n_k^0 + \frac{\partial n_k^0}{\partial \varepsilon_k} \left[\mu_m(y) + \sum_{n=1}^{\infty} g^{(n)}(y) P_n(\cos \theta) \right], \quad (8)$$

where $\varepsilon_k = \hbar\omega_k$ is the magnon energy, $\mu_m(y)$ is the $n = 0$ component of the small deviation and plays the role of a chemical potential, θ is the angle between \vec{k} and the y axis, and P_n is the Legendre polynomial of order n . Using the orthogonality relations for P_n , it has been shown that the magnon accumulation and the spin current are related to the deviations of the equilibrium distribution by [53,54]

$$\delta n_m(y) = I_0 \mu_m(y), \quad (9)$$

$$J_{S\delta n}^z(y) = \frac{\hbar}{3} I_1 g^{(1)}(y), \quad (10)$$

where the integrals are defined by

$$I_n = \frac{1}{(2\pi)^3} \int d^3k v_k^n \frac{\partial n_k^0}{\partial \varepsilon_k}. \quad (11)$$

In Refs. [53,54], it is shown that in the steady state, the magnon accumulation obeys a diffusion equation,

$$\frac{\partial^2 \delta n_m(y)}{\partial y^2} = \frac{\delta n_m(y)}{l_m^2}, \quad (12)$$

and that the spin current due to the spatial variation of the magnon accumulation is given by

$$J_{S\delta n}^z(y) = \hbar D_m \frac{\partial}{\partial y} \delta n_m(y), \quad (13)$$

where

$$D_m = \tau_m l_2 / (3I_0) \quad \text{and} \quad l_m = (D_m \tau_{\text{SL}})^{1/2} \quad (14)$$

are the diffusion parameter and diffusion length, respectively; τ_m is a weighted magnon lifetime averaged over the Brillouin zone; and τ_{SL} the spin-lattice relaxation time. The solution of Eq. (12) gives for the spatial variation of the magnon accumulation

$$\delta n_m(y) = A \cosh[(y + t_{\text{FM}})/l_m] + B \sinh[(y + t_{\text{FM}})/l_m], \quad (15)$$

where A and B are coefficients to be determined by the boundary conditions. Using Eq. (15) in Eq. (13), one obtains the total y component of the z -polarized magnon spin-current density in the FMI:

$$J_S^m(y) = -S_S^z \nabla_y T + \hbar \frac{D_m}{l_m} A \sinh[(y + t_{\text{FM}})/l_m] + \hbar \frac{D_m}{l_m} B \cosh[(y + t_{\text{FM}})/l_m]. \quad (16)$$

This result will be used in the next section to match the boundary conditions at the free FMI surface and at the FMI/NM interface.

III. SPIN CURRENT AND ISHE VOLTAGE IN THE FMI/NM BILAYER

In this section, we consider the FMI layer in atomic contact with a NM having a strong spin-orbit scattering, such as Pt and Pd. As is well known, the precessing spins associated with the magnon accumulation at the FMI/NM interface pump a spin current into the NM given by [55,56]

$$\vec{J}_S^{sp}(0^+) = \frac{\hbar g_r^{\uparrow\downarrow}}{4\pi M^2} \left(\vec{M} \times \frac{\partial \vec{M}}{\partial t} \right), \quad (17)$$

where \vec{M} is the FMI magnetization at the interface and $g_r^{\uparrow\downarrow}$ is the real part of the spin mixing conductance. The spin current in the NM is carried by the conduction electrons and can be expressed in terms of a spin accumulation. The nonequilibrium spin accumulation builds up in the NM, resulting in a backflow spin current J_S^{bf} into the FMI. The spin accumulation is governed by a diffusion equation, which can be easily solved to calculate J_S^{bf} , considering the reflection at the surface in $y = t_N$. One can show that the sum of the y components of the z -polarized spin pump and backflow spin currents at the FMI/NM interface is $J_S^z(0^+) = -\hbar g_{\text{eff}}^{\uparrow\downarrow} / (4\pi M^2) \sum_k \omega_k (m_k^+ m_k^-)$, where m_k^+ and m_k^- are the circular polarized transverse components of the

magnetization associated with the k magnon and $g_{\text{eff}}^{\uparrow\downarrow}$ is the real part of the effective spin mixing conductance that takes into account the spin-pumped and backflow currents. In the linear approximation, $m_k^+ m_k^- \approx 2M \gamma \hbar \delta n_k / V$, so the spin current in the NM can be related to the magnon number (in excess of thermal equilibrium) at the interface

$$J_S^z(0^+) = -\frac{\gamma \hbar^2 g_{\text{eff}}^{\uparrow\downarrow}}{2\pi M} \frac{1}{(2\pi)^3} \int d^3 k \omega_k \delta n_k. \quad (18)$$

Using the expansion in Eq. (8) and the orthogonality relations for the Legendre polynomials, we find that only the $n = 0$ term contributes to Eq. (18). With Eq. (9) and $\partial n_k^0 / \partial \varepsilon_k = -e^x (e^x - 1)^{-2} (k_B T)^{-1}$, one can show that the spin current in the NM is related to the magnon accumulation at the interface by

$$J_S(0^+) = -\frac{\gamma \hbar k_B T}{2\pi M} \frac{C_1}{C_0} g_{\text{eff}}^{\uparrow\downarrow} \delta n_m(0), \quad (19)$$

where

$$C_1 = \int d^3 k \frac{x e^x}{(e^x - 1)^2} \quad \text{and} \quad C_0 = \int d^3 k \frac{e^x}{(e^x - 1)^2}. \quad (20)$$

In order to calculate the coefficients in Eq. (15) and the magnon accumulation $\delta n_m(0)$ at the FMI/NM interface in terms of the temperature gradient ∇T , we use the boundary conditions determined by conservation of the angular momentum flow that requires continuity of the spin currents at the interfaces [53–56,66]. At the substrate/FMI interface, $J_S^z(y = -t_{\text{FM}}) = 0$, whereas at the FMI/NM interface, $J_S^z(y = 0^-) = J_S^z(y = 0^+)$. From the boundary condition at $y = -t_{\text{FM}}$, we obtain, with Eq. (16), $B = S_S^z \nabla T l_m / \hbar D_m$. Using this result in Eq. (15), we find a relation between the coefficient A and the magnon accumulation at the FMI/NM interface:

$$A = \frac{\delta n_m(0)}{\cosh(t_{\text{FM}}/l_m)} - \frac{S_S^z \nabla T l_m}{\hbar D_m} \tanh(t_{\text{FM}}/l_m). \quad (21)$$

With the boundary condition $J_S^z(0^-) = J_S^z(0^+)$, where $J_S^z(0^-)$ is given by Eq. (16), with the coefficients A and B above, and $J_S^z(0^+)$ given by Eq. (19), we obtain the magnon accumulation at the FMI/NM interface created by the temperature gradient ∇T in the y direction:

$$\delta n_m(0) = \frac{1 - \cosh^{-1}(t_{\text{FM}}/l_m)}{a \tanh(t_{\text{FM}}/l_m) + b g_{\text{eff}}^{\uparrow\downarrow}} S_S^z \nabla T, \quad (22)$$

where

$$a = \hbar D_m / l_m \quad \text{and} \quad b = \gamma \hbar k_B T C_1 / (2\pi M C_0). \quad (23)$$

As will be shown in the next section, in YIG/Pt bilayers $a \gg b g_{\text{eff}}^{\uparrow\downarrow}$. Therefore, the spin-current density at the interface calculated with Eqs. (19) and (22) becomes approximately

$$J_S^z(0) = -\frac{b g_{\text{eff}}^{\uparrow\downarrow} \rho}{a} S_S^z \nabla T, \quad (24)$$

where ρ is a factor that represents the effect of the finite FMI layer thickness, given as

$$\rho = \frac{\cosh(t_{\text{FM}}/l_m) - 1}{\sinh(t_{\text{FM}}/l_m)}, \quad (25)$$

such that $\rho \approx 1$ for $t_{\text{FM}} \gg l_m$ and $\rho \approx 0$ for $t_{\text{FM}} \ll l_m$. Equation (24) shows that the magnon spin current at the FMI/NM interface generated by the temperature gradient applied perpendicularly to the bilayer plane is proportional to the temperature gradient and to the spin mixing conductance of the interface. This means that the NM layer in contact with the FMI film that is used to detect the ISHE voltage is essential for the existence of the spin current. This result explains the experimental observation [21,23,24] that a Pt layer in contact with a YIG film is necessary for using the SSE to control the relaxation rate of spin waves in the film.

In the experiments with the LSSE, one applies a temperature difference between the two sides of a FMI/NM bilayer to create a spin current across the structure using the arrangement illustrated in Fig. 3(a). Due to the ISHE, the spin-current density \vec{J}_S^z flowing into the NM layer generates a charge-current density given by $\vec{J}_C = \theta_{\text{SH}}(2e/\hbar)\vec{J}_S^z \times \vec{\sigma}$, where θ_{SH} is the spin-Hall angle and $\vec{\sigma}$ is the spin polarization [49]. If the magnetic field is applied in the plane and transverse to the long direction of the NM layer, the resulting charge current flows along the long direction and produces a direct current (dc) ISHE voltage at the ends of the NM layer. Since the spin current at the FMI/NM interface diffuses into the NM layer [53–56] with diffusion length λ_N , in order to calculate the voltage at the ends of the NM layer, one has to integrate the charge-current density along x and y so that the ISHE voltage becomes [51]

$$V = R_N w \lambda_N \frac{2e}{\hbar} \theta_{\text{SH}} \tanh\left(\frac{t_N}{2\lambda_N}\right) J_S^z(0), \quad (26)$$

where R_N , t_N , and w are the resistance, thickness, and width of the NM strip, respectively.

IV. APPLICATION TO YIG/PT BILAYERS

In order to calculate the integrals in Eqs. (7) and (20), one needs the relation between the spin-wave angular frequency ω_k and the wave number k . As is often done in the literature, we consider initially a quadratic dispersion relation $\omega_k = \omega_0 + \gamma Dk^2$, where ω_0 is the $k = 0$ magnon frequency and D is the intraexchange stiffness parameter. With the magnon velocity $v_k = \partial\omega_k/\partial k = 2\gamma Dk$, we obtain from Eq. (7)

$$S_S^z = C_{5/2} \frac{k_B^{5/2} T^{3/2} \tau_m}{6\pi^2 \hbar^{3/2} (\gamma D)^{1/2}}, \quad (27)$$

where $C_{5/2}$ is a parameter given by

$$C_{5/2} = \int \frac{e^x}{(e^x - 1)^2} x(x - x_0)^{3/2} dx, \quad (28)$$

where $x_0 = \hbar\omega_0/k_B T$. The lower limit of integration is x_0 , the minimum normalized spin-wave energy, determined by the magnetic field. The upper limit is the maximum energy at the Brillouin zone boundary. If we set $x_0 = 0$ and consider the upper limit infinity, since the integrand vanishes for large x , it can be shown that $C_{5/2} = \Gamma(7/2)\zeta(5/2) \approx 4.46$, where $\Gamma(z)$ and $\zeta(z)$ are the gamma and Riemann zeta functions, respectively. For fields up to a few kilooersteds, x_0 is small and the numerical integration of Eq. (8) gives a value close to the ones above. One can show that with the quadratic dispersion

relation, the diffusion parameter in Eq. (14) becomes

$$D_m = \frac{4\tau_m k_B T \gamma D C_{3/2}}{3\hbar C_{1/2}}, \quad (29)$$

where

$$C_{1/2} = \int dx \frac{e^x(x - x_0)^{1/2}}{(e^x - 1)^2} \quad \text{and} \quad C_{3/2} = \int dx \frac{e^x(x - x_0)^{3/2}}{(e^x - 1)^2}. \quad (30)$$

If we set $x_0 = 0$ and consider the upper limit infinity, it can be shown that $C_{3/2} = \Gamma(5/2)\zeta(3/2) \approx 3.4$. For $x_0 \neq 0$, numerical integration shows that this value changes little for fields of a few kilooersteds. The situation is different for $C_{1/2}$, because the integration diverges for $x_0 = 0$. Considering $H = 100$ Oe, $x_0 = 4.2 \times 10^{-5}$, numerical integration gives $C_{1/2} \approx 250$. Using $a = \hbar(D_m/\tau_{\text{SL}})^{1/2}$, $b = \gamma \hbar k_B T C_{3/2}/(2\pi M C_{1/2})$, and S_S^z given by Eq. (27), the spin current at the interface in Eq. (24) becomes, for $\rho = 1$,

$$J_S^z(0) = \frac{(k_B T)^2 (3\tau_{\text{SL}}\tau_m)^{1/2}}{4\pi M D 6\pi^2 \hbar} \left(\frac{C_{3/2}}{C_{1/2}}\right)^{1/2} C_{5/2} g_{\text{eff}}^{\uparrow\downarrow} k_B \nabla T. \quad (31)$$

We use for YIG the following parameters [62]: $\gamma = 1.76 \times 10^7 \text{ s}^{-1}$, $D = 5.4 \times 10^{-9} \text{ Oe cm}^2$, $4\pi M = 1.76 \text{ kG}$, $\tau_{\text{SL}} \approx 10^{-6} \text{ s}$, and $\tau_m \approx 10^{-10} \text{ s}$, which is an approximate average value for the magnon lifetime as calculated in the Appendix. The reported [61,63–67] values for the spin mixing conductance $g_{\text{eff}}^{\uparrow\downarrow}$ in YIG/Pt vary from $2 \times 10^{12} \text{ cm}^{-2}$ to $4 \times 10^{14} \text{ cm}^{-2}$. Considering $g_{\text{eff}}^{\uparrow\downarrow} = 10^{14} \text{ cm}^{-2}$, we find from Eq. (31) for $\nabla T = 300 \text{ K/cm}$ and $T = 300 \text{ K}$ a spin-current density at the interface $J_S(0) \approx 10^{-4} \text{ erg/cm}^2$. Using for Pt [51,65–71] $\lambda_N = 4 \text{ nm}$, $\theta_{\text{SH}} = 0.08$, and conductivity $\sigma_{\text{Pt}} = 2.4 \times 10^4 \Omega^{-1} \text{ cm}^{-1}$, the resistance of a Pt strip with typical dimensions $l = 0.6 \text{ cm}$, $w = 0.2 \text{ cm}$, and $t_N = 6 \text{ nm}$ is $R_N = 208 \Omega$, and we obtain from Eq. (26) an ISHE voltage of $V \approx 40 \text{ mV}$. This is more than three orders of magnitude larger than the experimental values [5,6,25].

The value of the spin current calculated with Eq. (31) is overestimated mainly because the quadratic magnon dispersion relation, which is widely used in calculations, deviates considerably from the actual relation for magnon with large wave numbers that have a strong weight in the integral in Eq. (28). This is clearly seen in Fig. 2, which shows the calculated dispersion relation for YIG [72] and the curve for $\omega_k = \omega_0 + \gamma Dk^2$. Two steps are taken to improve the calculation. First, we use for the magnon dispersion relation

$$\omega_k = \omega_{\text{ZB}} \left(1 - \cos \frac{\pi k}{2k_m}\right), \quad (32)$$

where ω_{ZB} is the zone boundary frequency and k_m is the value of the maximum wave number. As shown in Fig. 2, Eq. (32) is a better approximation for the magnon dispersion over the whole Brillouin zone. Second, we take into account that the magnon lifetime is a strong function of the wave number, as shown in the appendix. With the dispersion in Eq. (32), the group velocity becomes $v_k = \omega_{\text{ZB}}(\pi/2k_m) \sin(\pi k/2k_m)$. Writing the magnon lifetime as $\tau_k = \tau_0/\eta_q$, where τ_0 is the lifetime of magnons near the zone center ($k \approx 0$) and

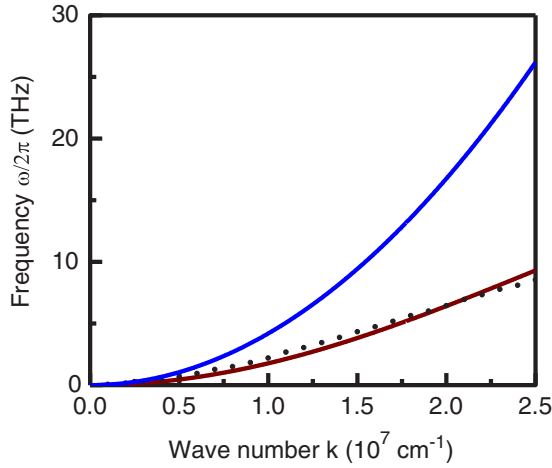


FIG. 2. (Color online) Spin-wave dispersion in YIG. The upper (blue) solid curve is calculated with quadratic dispersion. The dotted curve is calculated by Ref. [72] for k along a [111] direction. The lower (wine) solid curve is calculated with the linear approximation used to calculate the integrals.

$\eta_q = \eta_k/\eta_0$ is an adimensional relaxation rate, Eq. (7) leads to

$$S_S^z = \frac{\hbar\tau_0 k_m \omega_{ZB}^2}{24T} B_S, \quad B_S = \int_0^1 dq q^2 \sin^2\left(\frac{\pi q}{2}\right) \frac{e^x x}{\eta_q (e^x - 1)^2}, \quad (33)$$

where $q = k/k_m$ is a normalized wave number. In Eq. (33), we consider spherical energy surfaces and integrate over a sphere of radius $k_m = \sqrt{3} \times 2.5/a_l$, a_l being the lattice parameter. One can show that with the dispersion relation in Eq. (32) and the wave number-dependent magnon relaxation rate, the diffusion coefficient in Eq. (14) becomes

$$D_m = \frac{\tau_0 \pi^2 \omega_{ZB}^2}{12k_m^2} \frac{B_2}{B_0}, \quad (34)$$

while the parameters in Eq. (23) are

$$a = \frac{\hbar\tau_0 \pi^2 \omega_{ZB}^2}{12k_m^2 l_m} \frac{B_2}{B_0} \quad \text{and} \quad b = \frac{\gamma \hbar k_B T}{2\pi M} \frac{B_1}{B_0}, \quad (35)$$

where

$$B_0 = \int_{q_0}^1 dq q^2 \frac{e^x}{(e^x - 1)^2}, \quad B_1 = \int_0^1 dq q^2 \frac{x e^x}{(e^x - 1)^2} \quad \text{and} \quad (36)$$

$$B_2 = \int_0^1 dq q^2 \sin^2\left(\frac{\pi q}{2}\right) \frac{e^x}{\eta_q (e^x - 1)^2}. \quad (37)$$

Using Eqs. (33)–(37) in Eq. (24), we obtain the following expression for the spin-current density at the FMI/NM interface:

$$J_S^z(0) = -\frac{\gamma \hbar \rho k_m^3 l_m}{4\pi M \pi^2} \frac{B_1 B_S}{B_2} g_{\text{eff}}^{\uparrow\downarrow} k_B \nabla T. \quad (38)$$

The integrals in Eqs. (33), (36), and (37) were evaluated numerically for YIG with the dispersion relation in Eq. (32),

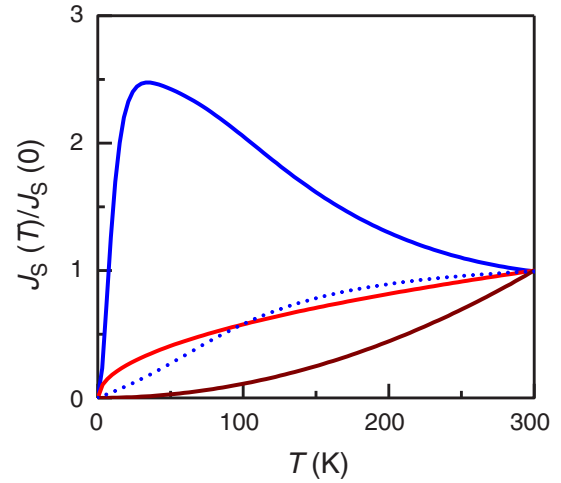


FIG. 3. (Color online) Temperature dependence of the spin current in the LSSE calculated with various models. The lower solid curve (wine) represents a T^2 dependence, as in Eq. (31). The solid curve in the middle (red) represents a $T^{1/2}$ dependence, predicted by the mechanism of interfacial thermal spin current [38]. The dotted and upper solid (blue) curves correspond to Eq. (38), calculated without and with, respectively, a temperature dependence in the magnon lifetime.

where $x = \hbar\omega_k/(k_B T)$, with $\omega_{ZB} = 6 \times 10^{13} \text{ s}^{-1}$, corresponding to the zone boundary frequency of 9.5 THz in Fig. 2. In the integral in B_0 , we consider a minimum normalized wave number $q_0 = 10^{-3}$ determined by the boundary conditions imposed by the contact with the Pt layer [68]. We also use for YIG a lattice parameter $a_l = 1.23 \text{ nm}$, which gives $k_m = 2 \times 10^7 \text{ cm}^{-1}$, and the normalized magnon relaxation rate calculated in the Appendix due to 3- and 4-magnon processes, $\eta_q = \eta_k/\eta_0 = 1 + (0.5q + 5.1q^2 - 3.25q^3) \times 10^3$. Hence, we find for $T = 300 \text{ K}$, $B_S = 2.2 \times 10^{-4}$, $B_0 = 282$, $B_1 = 0.55$, and $B_2 = 5.1 \times 10^{-3}$. With these values and $\tau_0 = 0.5 \times 10^{-7} \text{ s}$, we obtain a diffusion coefficient $D_m = 6.6 \text{ cm}^2/\text{s}$. Considering [54] $\tau_{\text{SL}} = 10^{-6} \text{ s}$, we find from Eq. (14) a magnon diffusion length $l_m = 26 \mu\text{m}$. These values will be used in the comparison of theory with experiments in the next section.

An important signature of a theoretical model for transport phenomena is the temperature dependence of physical quantities of interest. Figure 3 shows curves for the temperature dependence of the spin currents calculated with various models relative to their values at $T = 300 \text{ K}$. The lower solid curve (wine) corresponds to Eq. (31) calculated with the quadratic dispersion relation and setting infinity for the upper limits of the integrals. In this case, the parameters in Eqs. (28) and (30) do not depend on the temperature and the spin current varies with T^2 . The solid curve in the middle (red) represents a $T^{1/2}$ dependence, which applies to the mechanism of interfacial thermal spin current, Eqs. (12) and (15) of Ref. [38], that was used to interpret the experimental data obtained with transverse SSE in FMI layers. In the case of the calculation with the nearly exact dispersion relation, Eq. (38), the temperature dependence is not a simple one; it is contained in Eqs. (33), (36), and (37) for the coefficients B_1 , B_2 , and B_S through the variable $x = \hbar\omega_k/k_B T$ and the magnon relaxation rate. The results of the calculation with Eq. (38), considering that

$l_m \propto D_m^{1/2}$, as in Eq. (14), are plotted in two ways: (1) the dotted curve (blue) is obtained assuming that the magnon relaxation does not vary with temperature, and (2) the upper solid curve (blue) was calculated considering that the magnon relaxation rate varies with T^2 , as shown in the Appendix, and the temperature dependence of the magnetization, given by $M(T)/M(0) = 1.0 - 0.3(T/300)^2$, which represents well the experimental data for YIG [73]. In both cases, the magnon spin current vanishes at $T = 0$ because the thermal magnon population vanishes. Since the magnon population decreases, whereas the lifetime increases, as T is lowered, the competition between the two factors results in the peak ~ 30 K, which is a characteristic feature of our model. As will be shown later, the temperature dependence of the Pt layer resistance attenuates the peak somewhat.

V. EXPERIMENTAL RESULTS AND COMPARISON WITH THEORY

In order to test some features of the theoretical model presented in the previous sections, we have carried out two sets of measurements of the dc ISHE voltage due to LSSE. In the first set, we have done measurements at room temperature using an arrangement similar to those of Uchida *et al.* [5,6,25] and Kikkawa *et al.* [26], as illustrated in Fig. 4(a). In the second set, which is crucial to test the model, we have done measurements as a function of the sample temperature. The FMI material is a pure single crystal YIG, and the NM material is a Pt thin layer, which is known to have reasonably large values for the spin-Hall angle and

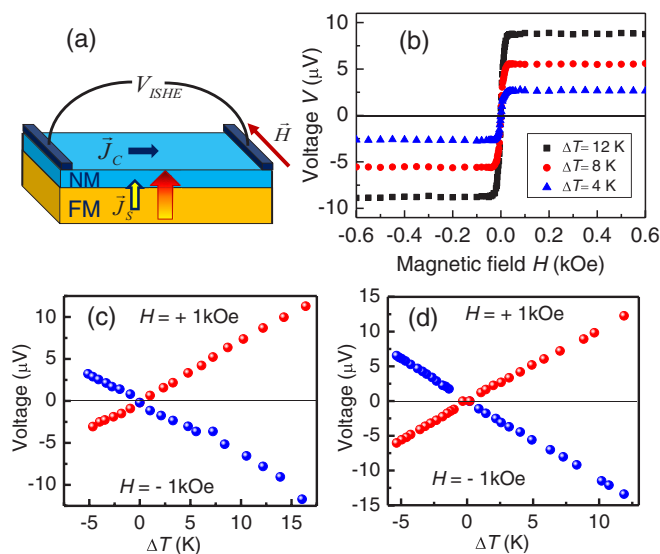


FIG. 4. (Color online) (a) FMI/NM bilayer used to study the LSSE. (b) Variation of the dc ISHE voltage V created by the SSE with the magnetic field intensity for three values of ΔT : 4, 8, and 12 K. (c) Variation of the voltage with the temperature difference ΔT between the two sides of sample A, consisting of a Pt (6 nm)/YIG (8 μm)/GGG (0.5 mm) structure. A positive ΔT corresponds to a temperature in the NM layer that is larger than in the FMI layer. (d) Variation of V with ΔT measured in sample B, consisting of a Pt (6 nm)/YIG (1 mm) slab.

spin mixing conductance with YIG. In the room-temperature measurements, a commercial Peltier module is used to heat or cool the side of the Pt layer, while the other side of the sample is in thermal contact with a copper block maintained at room temperature. The temperature difference across the sample is calibrated as a function of the current in the Peltier module by means of two thermocouples attached to thin copper sheets placed between the module and the sample structure. Two samples were used, designed to test the thickness dependence of the ISHE voltage. Sample A consists of a strip of single-crystal YIG (111) film grown by liquid phase epitaxy onto a 0.5-mm-thick [111]-oriented $\text{Gd}_3\text{Ga}_5\text{O}_{12}$ (GGG) substrate. Growth was made at a constant temperature in supersaturated solutions using a $\text{PbO-B}_2\text{O}_3$ -based flux by the horizontal dipping technique. The strip is 10 mm long and 2.3 mm wide, and the YIG film is 8 μm thick, with the thickness measured directly with a scanning electron microscope. The YIG strip is covered with a 6-nm-thick Pt layer deposited by magnetron sputtering. Two Cu wires attached with silver paint to the ends of the Pt layer are used to measure dc ISHE voltage directly with a nanovoltmeter. Sample B consists of a single-crystal YIG slab with the dimensions 10, 3, and 1 mm, cut with faces along (111) from a boule grown by the Czochralski method. The faces are optically polished, and one of them is fully covered with a 6-nm-thick Pt layer. The aim of using the two samples is to compare the dc ISHE voltages in an 8- μm -thick YIG film and in a 1-mm-thick single-crystal YIG slab measured with the same setup. Since the predicted magnon diffusion length is 26 μm , this would provide a test for the calculated variation of the LSSE with the YIG layer thickness.

Figure 4(b) shows the dependence of the voltage created by the spin current due to the SSE on the magnetic field intensity (applied perpendicularly to the ISHE current direction) for three values of the temperature difference ΔT across the Pt/YIG/GGG structure: 4, 8, and 12 K. The change in the sign of the voltage with the reversal in the direction of the field is due to the change in the sign of the spin polarization. The data show that for a fixed field direction, V does not depend on the value of the magnetic field, in agreement with the model. Figure 4(c) shows the measured variation of the voltage V in sample A with the temperature difference ΔT for an applied field $H = \pm 1$ kOe. The linear dependence of V on ΔT confirms the prediction of Eqs. (26) and (38). Figure 4(d) shows the variation of V with ΔT measured in sample B. Since the thicknesses of the Pt/YIG/GGG structure and of the Pt/YIG slab are 0.5 and 1.0 mm, respectively, for a given ΔT , the temperature gradient ∇T is twice as large in the former as in the latter. One important conclusion drawn from the data of Fig. 4(c) and 4(d) is that the voltage due to the SSE spin current in an 8- μm -thick YIG film is comparable to that in a 1-mm-thick YIG slab. In other words, for a fixed temperature gradient, V is independent of the FMI layer thickness in the thickness range of the measurements. This result seems to contradict the predictions of the model in Eq. (38), since sample A has $t_{\text{FM}} \ll l_m$ and the factor expressing the influence of FMI thickness in Eq. (25) is $\rho \ll 1$, while sample B has $t_{\text{FM}} \gg l_m$ and consequently $\rho \approx 1$. However, while the original version of this paper was in the review process, the authors learned of the recent measurements by Kehlberger *et al.*

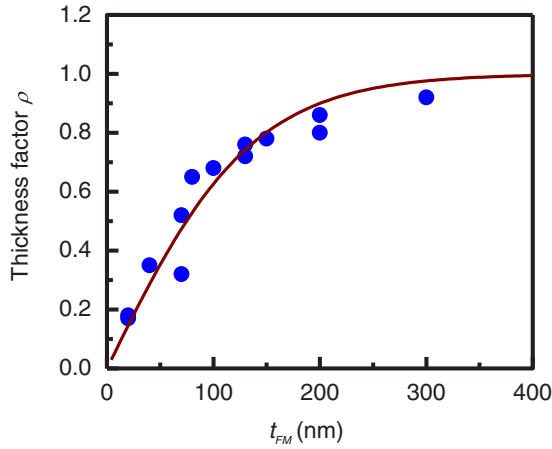


FIG. 5. (Color online) Symbols represent data of Ref. [57] for the normalized LSSE for three series of YIG(t_{FM})/Pt bilayers. The solid line is a least-square deviation fit with Eq. (25).

of the YIG thickness dependence of the LSSE in YIG/Pt bilayers done with very thin YIG layers [57].

Figure 5 shows data of Ref. [57] for the LSSE measured by the ISHE voltage in three series of YIG/Pt bilayers with varying YIG thickness normalized to the corresponding values at large thicknesses. This normalized quantity corresponds precisely to the thickness factor ρ of our model. We have used the same symbol to represent the data obtained with the three series of sample. The solid line in Fig. 5 represents a least-square deviation fit of Eq. (25) to the data, which yields a magnon diffusion length $l_m = 70$ nm. The possible explanation for this small diffusion length compared to the one calculated before with Eq. (14) is that its relation with the diffusion coefficient should involve the magnon lifetime and not the spin-lattice relaxation time. In fact, with $l_m = 70$ nm and $D_m = 6.6$ cm²/s, we obtain $l_m^2/D_m \approx 0.7 \times 10^{-10}$ s, which is on the same order of magnitude of the averaged magnon lifetime calculated in the Appendix.

Now we can use Eq. (38) to calculate the spin-current density created by a given temperature difference ΔT across a YIG/Pt bilayer. For $\Delta T = 15$ K in a sample that is 0.5 mm thick, the temperature gradient is $\nabla T = 300$ K/cm. Using $l_m = 70$ nm, $k_m = 2 \times 10^7$ cm⁻¹, $B_S = 2.2 \times 10^{-4}$, $B_1 = 0.55$, $B_2 = 5.1 \times 10^{-3}$, $4\pi M = 1.76$ kG, $\gamma = 1.76 \times 10^7$ s⁻¹ Oe⁻¹, and $g_{\text{eff}}^{\uparrow\downarrow} = 2 \times 10^{14}$ cm⁻², for $t_{\text{FM}} \gg l_m$ and $T = 300$ K, Eq. (38) gives a spin-current density $J_S^z(0) \approx 10^{-8}$ erg/cm². Using this value for the spin-current density in Eq. (26); the parameters for Pt of $\lambda_N = 4$ nm, $\theta_{\text{SH}} = 0.08$, and $w = 0.2$ cm; and the measured resistance $R_N = 166\Omega$, we obtain a voltage $V \approx 5\mu\text{V}$, which is on the order of magnitude agreement with the experimental values.

The second set of experiments was conducted to test a crucial feature of the model: the dependence of the ISHE voltage on the sample temperature. A sample made of a strip of Pt (6 nm)/YIG (8 μm)/GGG (0.5 mm) prepared similarly to sample A, as described earlier, was mounted directly on the copper base of a Displex closed cycle cryostat and glued with General Electric varnish. The temperature gradient is created by heating the Pt side with a heater, made

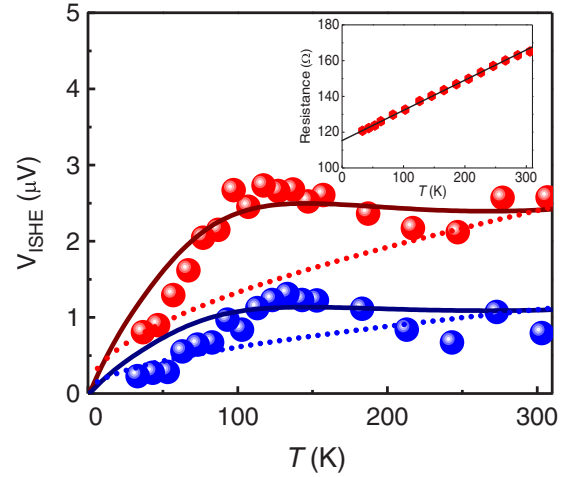


FIG. 6. (Color online) Comparison of the experimental data with calculated temperature dependence of ISHE voltage V created by the LSSE in YIG/Pt. The symbols represent the voltage measured with $\Delta T = 3$ K (blue) and 7 K (red). The dotted lines are calculated with the interfacial thermal spin pumping mechanism [38], while the solid lines are calculated with the magnon spin-current model presented here. The inset shows the measured resistance of the Pt layer and the linear fit used in the calculation of the voltage.

of a resistive wire in zigzag between two sheets of Kapton (polyimide), while the opposite GGG side is maintained at the base temperature T_b of the cryostat. The temperature difference ΔT across the Pt/YIG/GGG structure was measured with a Cu-constantan-Cu differential thermometer made of two thermocouple junctions, one in contact with a thin copper strip placed between the heater and the Pt layer and the other in contact with the base. The Pt/YIG temperature used to plot the data is $T = T_b + \Delta T$, where T_b is the cryostat base temperature. The ISHE voltage was measured with a nanovoltmeter by means of two Cu wires attached with silver paint to the ends of the Pt layer. The Cu wires were also used to measure the resistance R_N of the Pt layer as a function of temperature. The symbols in Fig. 6 represent the ISHE voltage measured with $\Delta T = 3$ and 7 K under a transverse magnetic field of $H = 1$ kOe. The residual contribution from contacts and pickup is removed by subtracting the voltages measured with the fields in opposite directions. In order to compare the data with the results of the model, it is necessary to take into account that the Pt layer resistance and the spin-Hall angle vary with T . The measurements shown in the inset of Fig. 6 are fit with $R_N(T) \approx R_N(300)[0.7 + 0.3(T/300)]$. Since there are no systematic data for the temperature dependence of the spin-Hall angle [67], we consider that the origin of R_N and the ISHE rely on the scattering of the conduction electrons in Pt and assume that $\theta_{\text{SH}}(T)$ follows the same T dependence as $R_N(T)$. The diffusion length λ_N also may vary with temperature. However, in the thickness range of our experiments, λ_N in the numerator of Eq. (26) approximately cancels out the one in the denominator of the tanh function. The curves in Fig. 6 were calculated with Eq. (26) using the spin currents shown in Fig. 3 and $R_N(T)$, $\theta_{\text{SH}}(T)$ above, adjusted to the measured ISHE voltages at $T = 300$ K. While the dotted lines representing the mechanism of interfacial thermal

spin pumping falling off with temperature much faster than with the data, the solid lines corresponding to the magnon spin-current model presented here are in good agreement with the experimental data.

In summary, we have shown that the mechanism behind the LSSE observed in bilayers made of a FMI and a NM relies on the bulk magnon spin current created by the temperature gradient across the thickness of the FMI. The spin current pumped into the NM layer provides continuity for the spin current at the FMI/NM interface, and it is essential for the existence of the SSE and its detection by the voltage created by the ISHE. The results of the model are in good quantitative agreement with the measured dependences of the ISHE voltage due to the LSSE in bilayers of YIG/Pt on the YIG thickness and on the sample temperature.

ACKNOWLEDGMENT

This paper was supported in Brazil by the Conselho Nacional de Desenvolvimento Científico e Tecnológico, Coordenação de Aperfeiçoamento de Pessoal de Nível Superior, Financiadora de Estudos e Projetos, and Fundação de Amparo à Ciência e Tecnologia do Estado de Pernambuco and in Chile by the Millennium Science Nucleus “Basic and Applied Magnetism” Contract No. P10-061-F and Fondo Nacional de Desarrollo Científico y Tecnológico Contract No. 1130705.

APPENDIX: CALCULATION OF THE MAGNON RELAXATION RATE IN YIG

The lifetime of magnon plays an important role in their transport properties. The relaxation rate, which is the inverse of the lifetime, has been investigated for low wave number magnons in YIG both theoretically and experimentally [62]. Detailed measurements of the relaxation rate have been made for magnons with wave numbers $k < 10^6 \text{ cm}^{-1}$ using microwave parametric pumping techniques [74]. In single-crystal YIG, the relaxation rate varies linearly with k and is the range $\eta_k \approx 10^6 - 10^8 \text{ s}^{-1}$ at room temperature. The data are well explained by 3-magnon relaxation processes [62] that predict a linear variation with k and with temperature, $\eta_{k3m} \propto kT$. However, the magnons that contribute most to the integrals appearing in the transport properties have larger wave numbers, and their relaxation rates have not been investigated in detail. Some experiments with large microwave frequencies [75,76] indicate that 4-magnon processes dominate the relaxation for $k > 10^6 \text{ cm}^{-1}$. The spin-wave relaxation due to 4-magnon processes has been investigated in antiferromagnets [77,78], which have data obtained with inelastic neutron scattering [79,80], but to the authors’ knowledge there are no experimental data or calculations for ferromagnets. Here, we present a calculation of the 4-magnon relaxation for YIG. The 4-magnon interaction Hamiltonian is dominated by the exchange interaction [62,77,78,81] that has parameters well characterized for YIG. The relaxation rate of a magnon with frequency ω_k and wave vector \vec{k} due to a process in which two magnons are annihilated and two magnons are created

is [77,78]

$$\eta_k = \frac{2\pi}{\hbar} (e^{\hbar\omega_1/k_B T} - 1) \sum_{k_2, k_3, k_4} |C_{1234}|^2 \times e^{\hbar\omega_2/k_B T} \bar{n}_{k_2} \bar{n}_{k_3} \bar{n}_{k_4} \Delta(k) \delta(\omega), \quad (\text{A1})$$

where $\Delta(k) = \Delta(\vec{k} + \vec{k}_2 - \vec{k}_3 - \vec{k}_4)$ and $\delta(\omega) = \delta(\omega_k + \omega_2 - \omega_3 - \omega_4)$ are the Kroenecker delta and the Dirac delta function of the momentum and energy conservation, respectively; \bar{n}_k is the occupation number of the k magnon given by the Bose-Einstein distribution; and C_{1234} is the interaction coefficient given by

$$C_{1234} = \frac{zJ}{2N} (\gamma_k + \gamma_{k_2} + \gamma_{k_3} + \gamma_{k_4} - 4\gamma_{k_4-k_2}), \quad (\text{A2})$$

where z and J are the nearest-neighbor number and exchange interaction constant, related to magnon zone boundary energy by $zJ = \hbar\omega_{ZB}/(4Sa_l)$; S is the spin per unit cell; N is the number of cells (with volume a_l^3); and $\gamma_k = \cos(\pi k/2k_m)$ is a geometric factor. The relaxation rate in Eq. (A1) was calculated numerically, similarly to what was done for antiferromagnets [78]. We assume spherical energy surfaces in the k space with a maximum radius k_m and dispersion relation $\omega_k = \omega_{ZB}(1 - \gamma_k)$, and we define $\vec{k}_S = \vec{k} + \vec{k}_2 = \vec{k}_3 + \vec{k}_4$ so that the energy delta function can be transformed as

$$\delta(\omega) = \frac{2k_m k_4 \delta(u - u_0)}{\omega_{ZB} \pi k_S k_3 \sin(\pi k_4/2k_m)}, \quad (\text{A3})$$

where $u = \cos \theta_3$, θ_3 being the angle between \vec{k}_3 and \vec{k}_S ; u_0 is the value of u for which energy is conserved $\omega_k + \omega_2 = \omega_3 + \omega_4$. The calculation proceeds as follows: The sum over k_4 is eliminated by momentum conservation, and the other sums are converted into integrals over the Brillouin zone with $\sum \rightarrow N\Omega/(2\pi)^3 \int d^3k$. Then the integrals over the azimuthal angles φ_3 and φ_4 are freely evaluated, giving $(2\pi)^2$, so that the relaxation rate becomes

$$\eta_{k1} = (e^{\hbar\omega_k/k_B T} - 1) \frac{N^2 a_l^6}{\hbar(2\pi)^3} \int k_2^2 dk_2 \int_{-\pi}^{\pi} \sin \theta_2 d\theta_2 \times \int k_3^2 dk_3 \int_{-1}^1 du \delta(u - u_0) |C_{1234}|^2 \bar{n}_{k_2} \bar{n}_{k_3} \bar{n}_{k_4} \times \frac{2k_m k_4}{\omega_{ZB} \pi k_S k_3 \sin(\pi k_4/2k_m)}. \quad (\text{A4})$$

The integrals in k_2 , k_3 , and θ_2 were evaluated numerically by coarse sums over a spherical Brillouin zone for a fixed temperature T and varying wave number k , or for fixed k and varying T . The sums were carried out by dividing the integration range in 300–1000 points, letting k_2 , k_3 , and θ_2 assume all possible values and considering to the sums only those values for which $|u_0| \leq 1$, where u_0 is calculated from $k_4^2 = k_2^2 + k_3^2 - 2k_S k_3 u_0$. The calculation reveals that the relaxation rate increases monotonically with k , but drops near the zone boundary. This drop can be eliminated by considering umklapp processes, in which the momentum conservation assumes the form $\vec{k} + \vec{k}_2 = \vec{k}_3 + \vec{k}_4 + \vec{G}$, where \vec{G} is a vector of the reciprocal lattice. The difficulty in defining \vec{G} in a spherical Brillouin zone is resolved by assuming it is either parallel or perpendicular to \vec{k} and has the amplitude $2k_m$.

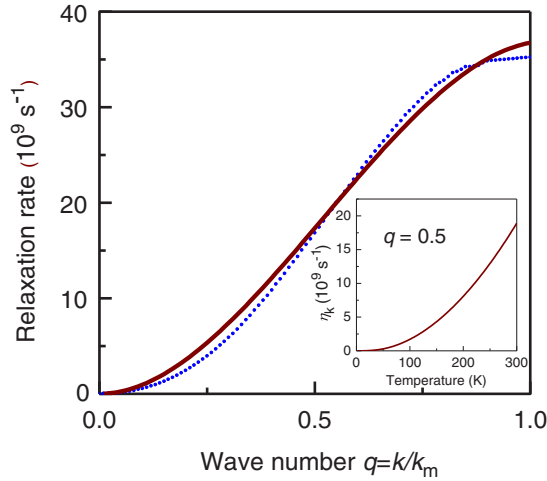


FIG. 7. (Color online) The dotted curve represents the calculated relaxation rate of magnons in YIG at $T = 300$ K as a function of the normalized wave number $q = k/k_m$. The solid curve is a polynomial fit. The temperature dependence of the relaxation rate for $q = 0.5$ is shown in the inset.

Figure 7 shows the calculated relaxation rate for magnons in YIG as a function of the wave number for $T = 300$ K. It

is noticeable that the relaxation rate for $k \sim 10^7$ cm $^{-1}$ is on the order of $\eta_k \sim 10^{10}$ s $^{-1}$, which corresponds to a magnon lifetime of $\tau_k \sim 10^{-10}$ s, much shorter than the values usually quoted in the literature [38,53,54]. In Fig. 7, we also show a polynomial fit to the calculated 4-magnon relaxation rate described by

$$\eta_{k4m} = (10.2q^2 - 6.5q^3) \times 10^{10} \text{ s}^{-1}. \quad (\text{A5})$$

Calculation of the relaxation rate for fixed k in the middle of the Brillouin zone shows that it varies with temperature approximately as $T^{2.2}$, as shown in the inset of Fig. 7. Considering 3- and 4-magnon processes, one can write the total magnon relaxation rate at $T = 300$ K as

$$\eta_k = (1.0q + 10.2q^2 - 6.5q^3) \times 10^{10} \text{ s}^{-1}, \quad (\text{A6})$$

where the coefficient of the 3-magnon term was obtained from experimental data at $q \sim 10^{-2}$. Considering a relaxation rate at the zone center $\eta_0 \sim 2 \times 10^7$ s $^{-1}$ and the temperature dependences of the 3- and 4-magnon relaxations, one can write

$$\eta_k = 1.0 + 500q \left(\frac{T}{300} \right) + (5100q^2 - 3250q^3) \left(\frac{T}{300} \right)^2, \quad (\text{A7})$$

which is the expression used in the integrations in Eqs. (33) and (37).

-
- [1] G. E. W. Bauer, E. Saitoh, and B. J. van Wees, *Nat. Mater.* **11**, 391 (2012).
- [2] K. Uchida, S. Takahashi, K. Harii, J. Ieda, W. Koshibae, K. Ando, S. Maekawa, and E. Saitoh, *Nature* **455**, 778 (2008).
- [3] K. Uchida, J. Xiao, H. Adachi, J. Ohe, S. Takahashi, J. Ieda, T. Ota, Y. Kajiwara, H. Umezawa, H. Kawai, G. E. W. Bauer, S. Maekawa, and E. Saitoh, *Nat. Mat.* **9**, 894 (2010).
- [4] K. Uchida, T. Ota, K. Harii, K. Ando, H. Nakayama, and E. Saitoh, *Solid State Comm.* **150**, 524 (2010).
- [5] K. Uchida, H. Adachi, T. Ota, H. Nakayama, S. Maekawa, and E. Saitoh, *Appl. Phys. Lett.* **97**, 172505 (2010).
- [6] K. Uchida, T. Nonaka, T. Ota, H. Nakayama, and E. Saitoh, *Appl. Phys. Lett.* **97**, 262504 (2010).
- [7] C. M. Jaworski, J. Yang, S. Mack, D. D. Awschalom, J. P. Heremans, and R. C. Myers, *Nat. Mater.* **9**, 898 (2010).
- [8] A. Slachter, F. L. Bakker, J. P. Adam, and B. J. van Wees, *Nat. Phys.* **6**, 879 (2010).
- [9] Y. Onose, T. Ideue, H. Katsura, Y. Shiomi, N. Nagaosa, and Y. Tokura, *Science* **329**, 297 (2010).
- [10] H. Yu, S. Granville, D. P. Yu, and J.-P. Ansermet, *Phys. Rev. Lett.* **104**, 146601 (2010).
- [11] S. Bosu, Y. Sakuraba, K. Uchida, K. Saito, T. Ota, E. Saitoh, and K. Takahashi, *Phys. Rev. B* **83**, 224401 (2011).
- [12] K. Uchida, H. Adachi, T. An, T. Ota, M. Toda, B. Hillebrands, S. Maekawa, and E. Saitoh, *Nat. Mater.* **10**, 737 (2011).
- [13] C. M. Jaworski, J. Yang, S. Mack, D. D. Awschalom, R. C. Myers, and J. P. Heremans, *Phys. Rev. Lett.* **106**, 186601 (2011).
- [14] K. Uchida, T. Ota, H. Adachi, J. Xiao, T. Nonaka, Y. Kajiwara, G. E. W. Bauer, S. Maekawa, and E. Saitoh, *J. Appl. Phys.* **111**, 103903 (2012).
- [15] E. Padrón-Hernández, A. Azevedo, and S. M. Rezende, *Phys. Rev. Lett.* **107**, 197203 (2011).
- [16] S. Y. Huang, W. G. Wang, S. F. Lee, J. Kwo, and C. L. Chien, *Phys. Rev. Lett.* **107**, 216604 (2011).
- [17] M. V. Costache, G. Bridoux, I. Neumann, and S. Valenzuela, *Nat. Mater.* **11**, 199 (2011).
- [18] M. Weiler, M. Althammer, F. D. Czeschka, H. Huebl, M. S. Wagner, M. Opel, I.-M. Imort, G. Reiss, A. Thomas, R. Gross, and S. T. B. Goennenwein, *Phys. Rev. Lett.* **108**, 106602 (2012).
- [19] C. M. Jaworski, R. C. Myers, E. Johnston-Halperin, and J. P. Heremans, *Nature* **487**, 210 (2012).
- [20] S. D. Brechet, F. A. Vetro, E. Papa, S. E. Barnes, and J. P. Ansermet, *Phys. Rev. Lett.* **111**, 087205 (2013).
- [21] L. Lu, Y. Sun, M. Jantz, and M. Wu, *Phys. Rev. Lett.* **108**, 257202 (2012).
- [22] G. L. da Silva, L. H. Vilela-Leão, S. M. Rezende, and A. Azevedo, *Appl. Phys. Lett.* **102**, 012401 (2013).
- [23] M. B. Jungfleisch, T. An, K. Ando, Y. Kajiwara, K. Uchida, B. I. Vasyuchka, A. V. Chumak, A. A. Serga, E. Saitoh, and B. Hillebrands, *Appl. Phys. Lett.* **102**, 062417 (2013).
- [24] R. O. Cunha, E. Padrón-Hernández, A. Azevedo, and S. M. Rezende, *Phys. Rev. B* **87**, 184401 (2013).
- [25] K. Uchida, T. Nonaka, T. Kikkawa, Y. Kajiwara, and E. Saitoh, *Phys. Rev. B* **87**, 104412 (2013).
- [26] T. Kikkawa, K. Uchida, Y. Shiomi, Z. Qiu, D. Hou, D. Tian, H. Nakayama, X.-F. Jin, and E. Saitoh, *Phys. Rev. Lett.* **110**, 067207 (2013).
- [27] T. An, V. I. Vasyuchka, K. Uchida, A. V. Chumak, K. Yamaguchi, K. Harii, J. Ohe, M. B. Jungfleisch, Y. Kajiwara, H. Adachi, B. Hillebrands, S. Maekawa, and E. Saitoh, *Nat. Mater.* **12**, 549 (2013).
- [28] W. Jiang, P. Upadhyaya, Y. Fan, J. Zhao, M. Wang, L.-T. Chang, M. Lang, K. L. Wong, M. Lewis, Y.-T. Lin, J. Tang, S. Cherepov,

- X. Zhou, Y. Tserkovnyak, R. N. Schwartz, and K. L. Wang, *Phys. Rev. Lett.* **110**, 177202 (2013).
- [29] B. F. Miao, S. Y. Huang, D. Qu, and C. L. Chien, *Phys. Rev. Lett.* **111**, 066602 (2013).
- [30] M. Agrawal, V. I. Vasyuchka, A. A. Serga, A. D. Karenowska, G. A. Melkov, and B. Hillebrands, *Phys. Rev. Lett.* **111**, 107204 (2013).
- [31] G. E. W. Bauer, A. H. MacDonald, and S. Maekawa, *Solid State Comm.* **150**, 459 (2010).
- [32] M. Hatami, G. E. W. Bauer, Q. Zhang, and P. J. Kelly, *Phys. Rev. B* **79**, 174426 (2009).
- [33] A. A. Kovalev and Y. Tserkovnyak, *Phys. Rev. B* **80**, 100408 (2009).
- [34] K. M. D. Hals, A. Brataas, and G. E. W. Bauer, *Solid State Comm.* **150**, 461 (2010).
- [35] M. Hatami, G. E. W. Bauer, S. Takahashi, and S. Maekawa, *Solid State Comm.* **150**, 480 (2010).
- [36] Z. Yuan, S. Wang, and K. Xia, *Solid State Comm.* **150**, 548 (2010).
- [37] J. C. Slonczewski, *Phys. Rev. B* **82**, 054403 (2010).
- [38] J. Xiao, G. E. W. Bauer, K. C. Uchida, E. Saitoh, and S. Maekawa, *Phys. Rev. B* **81**, 214418 (2010).
- [39] G. E. W. Bauer, S. Bretzel, A. Brataas, and Y. Tserkovnyak, *Phys. Rev. B* **81**, 024427 (2010).
- [40] Y. Takezoe, K. Hosono, A. Takeuchi, and G. Tatara, *Phys. Rev. B* **82**, 094451 (2010).
- [41] J. Sinova, *Nat. Mat.* **9**, 880 (2010).
- [42] D. Hinzke and U. Nowak, *Phys. Rev. Lett.* **107**, 027205 (2011).
- [43] H. Adachi, J. I. Ohe, S. Takahashi, and S. Maekawa, *Phys. Rev. B* **83**, 094410 (2011).
- [44] J. I. Ohe, H. Adachi, S. Takahashi, and S. Maekawa, *Phys. Rev. B* **83**, 115118 (2011).
- [45] H. Adachi, K. Uchida, E. Saitoh, and S. Maekawa, *Rep. Prog. Phys.* **76**, 036501 (2013).
- [46] Y. Ohnuma, H. Adachi, E. Saitoh, and S. Maekawa, *Phys. Rev. B* **87**, 014423 (2013).
- [47] S. Hoffman, K. Sato, and Y. Tserkovnyak, *Phys. Rev. B* **88**, 064408 (2013).
- [48] A. Azevedo, L. H. Vilela-Leão, R. L. Rodríguez-Suárez, A. B. Oliveira, and S. M. Rezende, *J. Appl. Phys.* **97**, 10C715 (2005).
- [49] E. Saitoh, M. Ueda, H. Miyajima, and G. Tatara, *Appl. Phys. Lett.* **88**, 182509 (2006).
- [50] O. Mosendz, V. Vlaminck, J. E. Pearson, F. Y. Fradin, G. E. W. Bauer, S. D. Bader, and A. Hoffmann, *Phys. Rev. B* **82**, 214403 (2010).
- [51] A. Azevedo, L. H. Vilela-Leão, R. L. Rodríguez-Suárez, A. F. Lacerda Santos, and S. M. Rezende, *Phys. Rev. B* **83**, 144402 (2011).
- [52] Z. Qiu, K. Ando, K. Uchida, Y. Kajiwara, R. Takahashi, H. Nakayama, T. An, Y. Fujikawa, and E. Saitoh, *Appl. Phys. Lett.* **103**, 092404 (2013).
- [53] Steven S.-L. Zhang and Shufeng Zhang, *Phys. Rev. Lett.* **109**, 096603 (2012).
- [54] Steven S.-L. Zhang and Shufeng Zhang, *Phys. Rev. B* **86**, 214424 (2012).
- [55] Y. Tserkovnyak, A. Brataas, and G. E. W. Bauer, *Phys. Rev. B* **66**, 224403 (2002).
- [56] Y. Tserkovnyak, A. Brataas, G. E. Bauer, and B. I. Halperin, *Rev. Mod. Phys.* **77**, 1375 (2005).
- [57] M. Weiler, M. Althammer, M. Schreier, J. Lotze, M. Pernpeintner, S. Meyer, H. Huebl, R. Gross, A. Kamra, J. Xiao, Y.-T. Chen, H. J. Jiao, G. E. W. Bauer, and S. T. B. Goennenwein, *Phys. Rev. Lett.* **111**, 176601 (2013).
- [58] A. Kehlberger, R. Röser, G. Jakob, M. Kläui, U. Ritzmann, D. Hinzke, U. Nowak, M. C. Onbasli, D. H. Kim, C. A. Ross, M. B. Jungfleisch, and B. Hillebrands, [arXiv:1306.0784](https://arxiv.org/abs/1306.0784) (2013).
- [59] M. Johnson and R. H. Silsbee, *Phys. Rev. B* **35**, 4959 (1987).
- [60] C. Heide, *Phys. Rev. Lett.* **87**, 197201 (2001).
- [61] Y. Kajiwara, K. Harii, S. Takahashi, J. Ohe, K. Uchida, M. Mizuguchi, H. Umezawa, K. Kawai, K. Ando, K. Takanashi, S. Maekawa, and E. Saitoh, *Nature (London)* **464**, 262 (2010).
- [62] M. Sparks, *Ferromagnetic Relaxation* (McGraw-Hill, New York, 1964).
- [63] C. H. Du, H. L. Wang, Y. Pu, T. L. Meyer, P. M. Woodward, F. Y. Yang, and P. C. Hammel, *Phys. Rev. Lett.* **111**, 247202 (2013).
- [64] C. Burrowes, B. Heinrich, B. Kardasz, E. A. Montoya, E. Girt, Y. Sun, Y.-Y. Song, and M. Wu, *Appl. Phys. Lett.* **100**, 092403 (2012).
- [65] V. Castel, N. Vlietstra, J. Ben Youssef, and B. J. van Wees, *Appl. Phys. Lett.* **101**, 132414 (2012).
- [66] V. Castel, N. Vlietstra, B. J. van Wees, and J. B. Youssef, *Phys. Rev. B* **86**, 134419 (2012).
- [67] A. Hoffmann, *IEEE Trans. Mag.* **49**, 5172 (2013).
- [68] S. M. Rezende, R. L. Rodríguez-Suárez, and A. Azevedo, *Phys. Rev. B* **88**, 014404 (2013).
- [69] L. Liu, T. Moriyama, D. C. Ralph, and R. A. Buhrman, *Phys. Rev. Lett.* **106**, 036601 (2011).
- [70] L. H. Vilela-Leão, C. Salvador, A. Azevedo, and S. M. Rezende, *Appl. Phys. Lett.* **99**, 102505 (2011).
- [71] S. M. Rezende, R. L. Rodríguez-Suárez, M. M. Soares, L. H. Vilela-Leão, D. Ley Domínguez, and A. Azevedo, *Appl. Phys. Lett.* **102**, 012402 (2013).
- [72] A. B. Harris, *Phys. Rev.* **132**, 2398 (1963).
- [73] M. A. Gilleo and S. Geller, *Phys. Rev.* **110**, 73 (1958).
- [74] S. M. Rezende and F. M. de Aguiar, *Proc. IEEE* **78**, 893 (1990).
- [75] A. G. Gurevich and A. N. Anisimov, *Zh. Eksp. Teor. Fiz.* **68**, 677 (1975).
- [76] A. N. Anisimov and A. G. Gurevich, *Fiz. Tverd. Tela* **18**, 38 (1976).
- [77] S. M. Rezende and R. M. White, *Phys. Rev. B* **14**, 2939 (1976).
- [78] S. M. Rezende and R. M. White, *Phys. Rev. B* **18**, 2346 (1978).
- [79] S. P. Bayrakci, T. Keller, K. Habicht, and B. Keimer, *Science* **312**, 1926 (2006).
- [80] S. P. Bayrakci, D. A. Tennant, Ph. Leininger, T. Keller, M. C. R. Gibson, S. D. Wilson, R. J. Birgeneau, and B. Keimer, *Phys. Rev. Lett.* **111**, 017204 (2013).
- [81] A. I. Akhiezer, V. G. Baryakhtar, and S. V. Peletminskii, *Spin Waves* (North Holland, Amsterdam, 1968).